Anal. Bioanal. Electrochem., Vol. 17, No. 7, 2025, 601-620
https://www.doi.org/10.22034/abec.2025.729837

Analytical & Bioanalytical Electrochemistry

2025 by CEE
www.abechem.com

Full Paper

Electrochemical Detection of Norepinephrine, Uric Acid, and L-Tyrosine using a Nanostructured Silver Manganese Oxide-MWCNT Electrode

Spoorthy R G, and Mamatha G P*

Department of Studies in Chemistry, Davangere University, Shivagangothri-577 007, Davangere, Karnataka, India

*Corresponding Author, Tel.: +91-9448422903
E-Mail: mamathagpgp2020@gmail.com

Received: 17 July 2025 / Received in revised form: 8 August 2025 /
Accepted: 16 September 2025 / Published online: 30 September 2025

Abstract- Silver manganese oxide (AMO) nanoparticles (Nnp) were synthesized using the co-precipitation method and characterized by X-ray diffraction (XRD), Fourier-transform infrared spectroscopy (FTIR), and scanning electron microscopy (SEM), (EDS) to confirm their structural and morphological properties. The synthesized AMO was incorporated with multi-walled carbon nanotubes (MWCNTs) to fabricate a modified glassy carbon electrode (GCE). This AMO-MWCNT Nnp composite electrode demonstrated remarkable efficiency for the simultaneous electrochemical detection of norepinephrine (NEP), uric acid (URA), and L-tyrosine (L-TY). Employing cyclic voltammetry (CV) and differential pulse voltammetry (DPV), the sensor exhibited excellent sensitivity and selectivity. Under optimal conditions, DPV was used for the simultaneous detection of NEP, URA, and L-TY at AMO Nnp-modified surfaces, achieving low detection limits of 4.04 nM for NEP, 3.01 nM for URA, and 10.31 nM for L-tyrosine. The synergistic effect of AMO Nnp and MWCNTs enhanced electron transfer kinetics, ensuring precise multi-analyte quantification. This work highlights the potential of the AMO-MWCNT Nnp modified electrode as a vigorous platform for advanced biomolecular sensing applications and real sample analysis.

Keywords- Multiwalled carbon nanotube composite; Norepinephrine; Uric acid; L-Tyrosine; Cyclic voltammetry; Differential pulse voltammetry; Co precipitation method

1. INTRODUCTION

Neurotransmitters are chemical messengers that transmit signals across chemical synapses, such as those between neurons or between neurons and muscles. They play a crucial role in the functioning of the nervous system by facilitating communication between cells. When an electrical signal reaches the end of a neuron, it triggers the release of neurotransmitters. Numerous brain processes including behaviour, cognition, circulatory, hormonal and renal systems depend heavily on neurotransmitters. In addition to influencing and regulating heart rate and muscle tone they also balance learning, memory, sleep, consciousness, mood and appetite. Numerous medical illnesses, neurodegenerative diseases, and psychotic disorders have been linked to changes in the concentration of neurotransmitters in the central nervous system. Neurotransmitters momentarily transform the electrical signals that move through the axon into chemical messages [1]. Neurotransmitter imbalances are linked to various health conditions including depression, anxiety, schizophrenia, and Parkinson's disease. Understanding how these chemicals work is key to developing treatments for these and other neurological disorders.

Norepinephrine (NEP), a metabotropic neurotransmitter released by the neuronal terminals of the adrenal medulla, the peripheral sympathetic nerves are an essential component of the central nervous systems of mammals. In addition to being essential for numerous physiological processes like memory, learning and the sleep-wake cycle, NEP also has an impact on individuals. Many disorders including ganglion neuronal, ganglia neuroblastoma, paraganglioma and Parkinson's disease. People's endogenous NEP levels when they are at rest are estimated to be between 150 and 800 ng/L. One of the important diagnostic markers for a few neurological disorders is thought to be the fluctuation in NEP concentration. Parkinson's disease and hypotension may result from low NEP levels, whereas paraganglioma and ganglia neuroblastoma are among the disorders linked to high NEP levels [2-9].

Uric acid (URA) is a crucial byproduct of metabolic purines and is primarily dissolved in human saliva, urine, plasma, and blood. In healthy individuals, the typical range for uric acid concentrations in saliva is 199 ± 27 μmol/L while serum concentrations are between 120–400 μmol/L [10]. The primary form of URA a weak acid is a urate salt at physiological pH [11]. The pathologic diseases of hyperuricemia and gout arise from the aberrant overproduction or underexcretion of urate, which causes its content in the blood to rise and crystallise. A risk indicator for cardiovascular disease is the rise in URA level in the blood, Lesch-Nyhan syndrome, kidney disease, hypertension, atherosclerosis, Alzheimer's disease, Parkinson's disease and other illnesses are all accompanied with elevated uric acid levels [12-17].

L-Tyrosine (L-TY) is an amino acid that plays a crucial role in the production of important substances in the body such as neurotransmitters and hormones. By serving as the building block for these neurotransmitters supports brain activity especially under stress or fatigue. Supplementing L-TY is often explored for its potential to enhance mental performance,

particularly in stressful situations [18,19]. It is an essential component of proteins which are necessary for establishing and preserving a positive nitrogen balance in human diet. Additionally, thyroxin, dopamine, dopa and epinephrine hormones or neurotransmitters are all precursors of tyrosine. Alkaptonuria and albinism may occur from a L-TY deficiency, whereas increased sister chromatid exchange is caused by a high L-TY concentration in the culture media. L-TY must thus be determined pharmacologically [20]. Various electrode types have recently been used for environmental monitoring and biological species identification. Chemically modified glassy carbon electrodes which are affordable and easily customisable with various nanoparticles were highlighted for their function. Electrochemical sensors with this kind of modification can be sensitive, reliable and repeatable [21-24].

As widely recognized, carbon nanotubes (CNTs) exhibit several exceptional properties, such as excellent electrical conductivity, remarkable chemical stability, a high aspect ratio and the ability to enhance electron-transfer reactions. Because of their special qualities CNTs are used in a wide range of industries including electronics, medicine and the aerospace sector. This has made analytical methods necessary to describe and regulate the quality of CNTs. Other fascinating developments in contemporary analytical research include the use of CNTs as analytical materials and the creation of CNT-based nanodevices and nano sensors. CNTs are now widely used in analytical chemistry including the creation of biosensors and electrochemical sensors. This work employed a quick and easy method to create an electrochemical sensor based on silver manganese oxide nanoparticles $AgMn_2O_4$ (AMO Nnp) and multiwalled carbon nanotubes (MWCNT) [25,26]. Because of their chemical stability, non-toxicity, abundance in nature and affordability. Nowadays carbon nanotubes are extensively used for the fabrication of sensors and biosensors because of their unique characteristics like high electrical and thermal conductivity, rich surface activity, hallow structure, absorption power [27] etc. Silver oxide nanoparticles which come in a variety of composition including Ag_2O, Ag_2O_3, and Ag_3O_4 are promising materials for sensor applications and various composition of manganese oxide nanomaterials such as MnO, MnO_2, and Mn_3O_4 are the most studied and beneficial candidates for electrode materials in electrochemical sensing, AMO-MWCNT Nnp modified glassy carbon electrode (MGCE) provides a good platform for the determination of NEP, UAR, and L-TY [28]. The electrochemical sensing studies were carried out by cyclic voltammetry (CV) and differential pulse voltammetry (DPV) techniques at AMO-MWCNT Nnp modified glassy carbon electrode. After several cycles, this fabricated material exhibited good stability and it was also successfully used to detect NEP, UAR, and L-TY simultaneously.

2. EXPERIMENTAL SECTION

2.1. Materials and devices utilized

All the chemicals used in the experiment, such as Silver Nitrate (Ag $(NO_3)_3.5H_2O$), Manganese Nitrate (Mn (NO_3)), Sodium Hydroxide (NaOH), NEP, UAR, L-TY, Sodium dihydrogen phosphate (NaH_2PO_4), and Disodium hydrogen phosphate (Na_2HPO_4) are purchased from Sigma–Aldrich. These chemicals are used without any purification and are of analytical grade. Distilled water (DI) is used for preparing all the required solutions.

All the Characterizations were performed at room temperature, and the instruments used are as follows: Rigaku Smart Lab X-ray diffractometer (XRD) was used for crystal structure analysis. Chemical bonding interactions were explored with the Cary 630 Agilent Technology FT-IR spectrophotometer. The surface morphology was analysed using (FESEM-CARLZEISS Ultra 55) Scanning electron microscope, and was used to describe the nanoparticle's size, shape, and internal structures. Elemental and trace elemental analyses were made by using EDAX (Oxford INCAx-act) and elemental mapping. A CHI-660E voltammetric analyser (CH-instrument-660E electrochemical workstation) was employed for CV, DPV, and LSV techniques. The electrolytic cell with a three-electrode system comprised of a counter electrode (platinum wire), a reference electrode (Ag/AgCl electrode in KCl), and working electrodes (bare and AMO-MWCNT Nnp modified glassy carbon electrodes).

2.2. Synthesis of AMO Nnp

The synthesis of AMO nanoparticles was carried out using the coprecipitation method. Equal volumes of 0.1 M silver nitrate ($Ag(NO_3)_2$) and manganese nitrate ($Mn(NO_3)_2$) solutions were mixed in a 1:1 molar ratio in an Erlenmeyer flask. The solution was stirred continuously for one hour, and the pH was carefully adjusted to pH 9 by adding 0.2 M sodium hydroxide (NaOH) dropwise while monitoring the pH. The mixture was maintained under continuous stirring and heating at 80^0C for six hours to ensure proper coprecipitation.

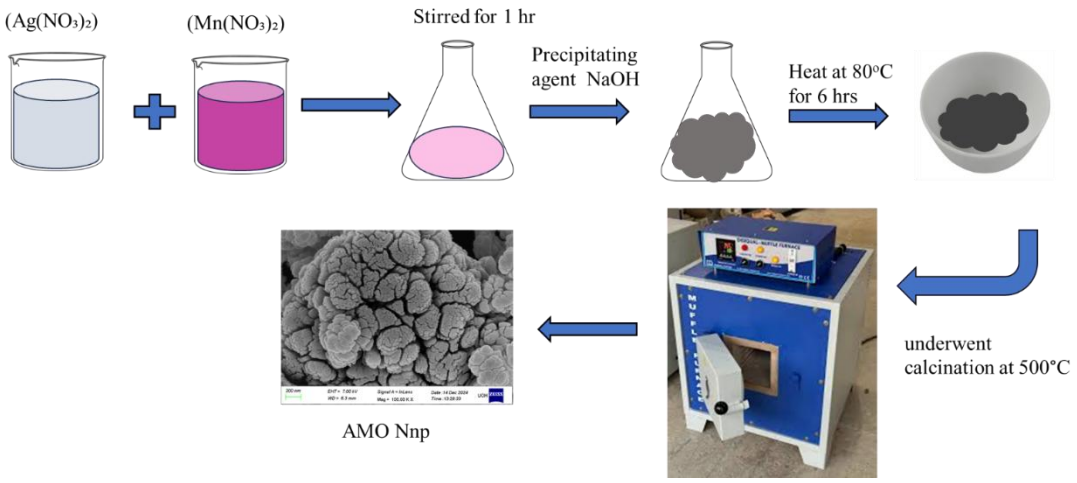

Scheme 1. Schematic diagram of the synthesis procedure of AMO Nnp

The resulting precipitate was then washed thoroughly with acetone and distilled water to remove impurities. After washing, the material was dried at 600°C for four hours to eliminate residual moisture. Finally, the dried material underwent calcination at 500^0C for two hours to obtain the desired AMO nanoparticle properties. This standardized protocol ensures a high-quality synthesis suitable for further applications.

3. RESULTS AND DISCUSSION

3.1. XRD analysis

AMO Nnp and AMO-MWCNT Nnp produced XRD patterns are displayed in Figure 1. The JCPDS file number 049-1259 well matches the diffraction peaks. The peaks at $2\theta = 29^0$, 32^0, 34.7^0, 37^0, 44^0, and 59^0 were indexed to the planes (002), (200), (110), (021), (201), (003), and (113), respectively. The resultant product displays single-phase crystallizing in a monoclinic system [29,30]. This demonstrates that AMO Nnp and AMO-MWCNT Nnp are formed as depicted in Figure 1. Additionally, it includes the peak at (002) that is found in the AMO-MWCNT Nnp; these are the multiwalled carbon nanotubes' principal peaks [31]. The diffraction peaks of AMO-MWCNT Nnp have a regulated breadth and good intensity, indicating that they are more crystalline than AMO Nnp. The Debye-Scherrer equation (1) was used to determine the average crystallite size of Nnp, and the results found to be 32 nm for AMO Nnp and 27 nm for AMO-MWCNT Nnp.

$$D = K \lambda / (\beta \cos \theta B) \quad (1)$$

Where D is the average crystallite size, β is the full width at half maximum (FWHM), λ is the X-ray wavelength (1.5405981 nm), θ is the Braggs diffraction angle and K is the dimensionless form factor shape particles [32].

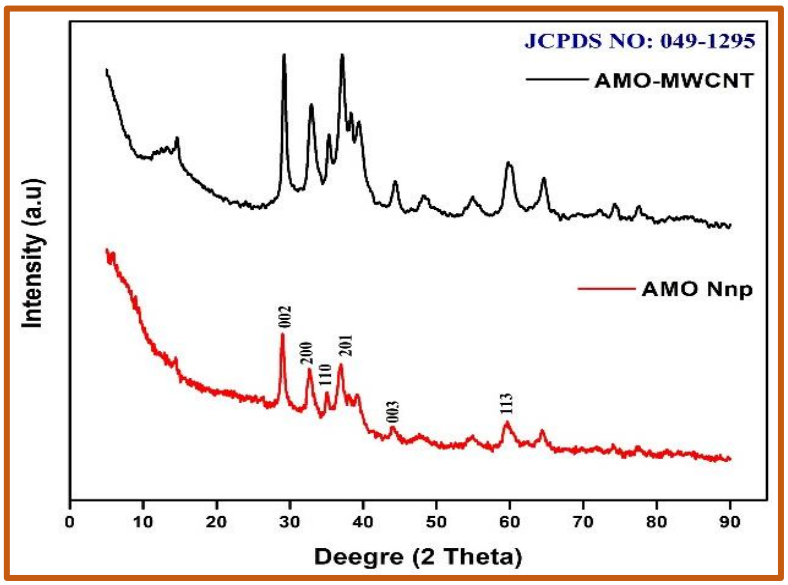

Figure 1. XRD patterns of AMO and AMO -MWCNT Nnp

3.2. FTIR analysis

FTIR of AMO Nnp and AMO-MWCNT nanoparticles are shown in Figure 2. Between 500 and 4000 cm^{-1} the samples' spectra were captured for both the fingerprint and high wavenumber regions. One vibrational spectroscopic approach that provides excellent information on both organic and inorganic chemicals, even when they are present in small amounts, is FT-IR. The primary vibrational bands for pure MnO_2 at 953, 1351, 1532, 1721, 3312,3549, and 3928 cm^{-1}. These bands are ascribed to Mn-O's bending vibrations from tetrahedral sites and stretching vibrations from octahedral sites. The vibration of the hydroxyl bond and the plane bending of the COO- bonding are shown by the bands at 1080 and 1304 cm^{-1}, respectively. Additionally, because of the high surface to volume ratio, the hydroxyl vibration bands (-OH) emerged at 1580 cm^{-1}, 2350 cm-1, and 3450 cm^{-1}. The prominent and broad peaks can be seen in AMO-MWCNT Nnp compared to AMO Nnp [33,34].

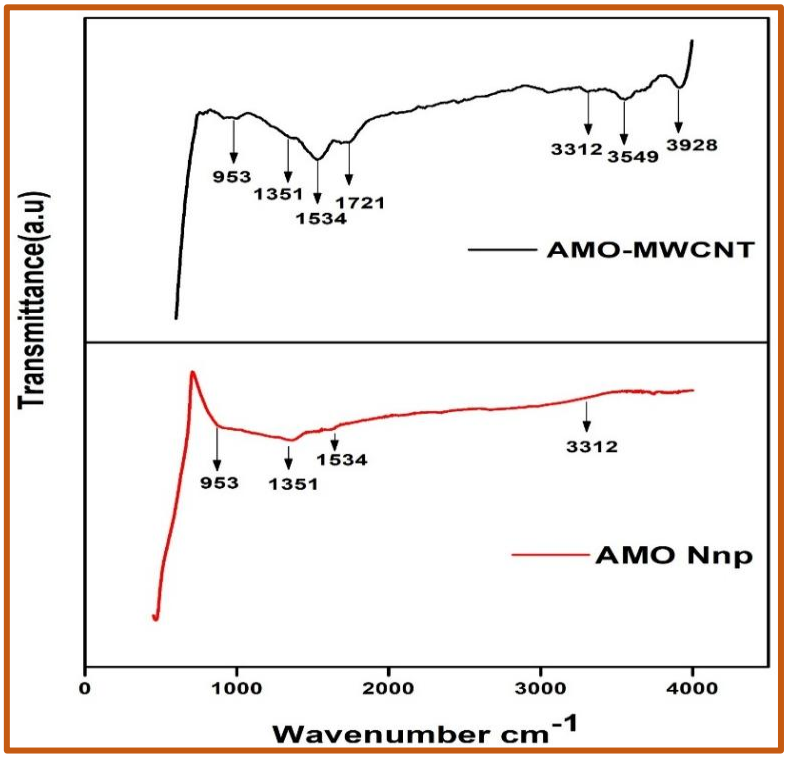

Figure 2. FTIR patterns of AMO and AMO-MWCNT Nnp

3.3. FESM and EDAX, Elemental mapping

FESEM micrographs were used to investigate the surface morphology of the prepared AMO Nnp and AMO-MWCNT Nnp. And the component composition was determined using EDX analysis and quantitative elemental mapping. This depicts the element's atomic proportion and existence in the absence of additional impurities. The EDX spectrum generated for AMO Nnp and AMO-MWCNT Nnp is shown in Figure 3 and Figure 4 which also demonstrates the presence and consistency of O, Ag and Mn, with atomic percentages, which

were used to estimate the basic composition of the prepared AMO and AMO-MWCNT. The elemental mapping using the colours blue, green, and red for the elements Ag, Mn, and O, and green, red, dark green, and blue for the elements Ag, Mn, O, C, respectively, confirmed the elements' equal distribution in the prepared AMO and AMO-MWCNT samples as shown in Figure 5 (a, b).

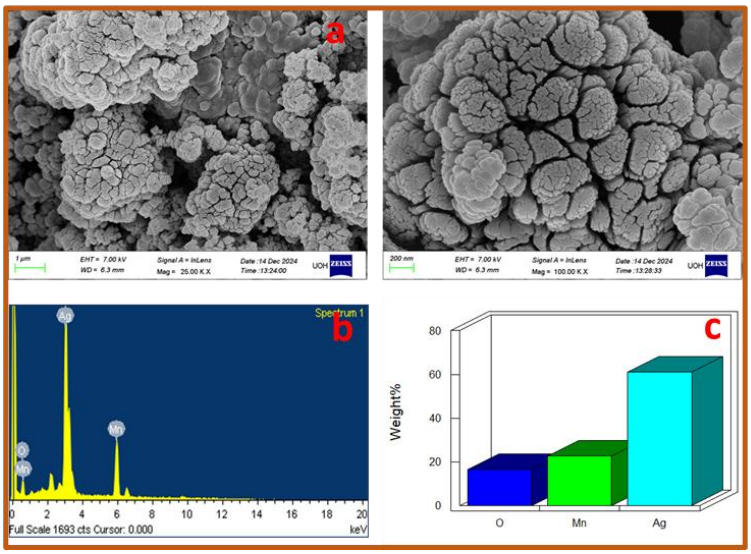

Figure 3. (a) FE-SEM images AMO Nnp, (b) EDS spectrum analysis of AMO Nnp, (c) image corresponding to Graphical representation of Elemental composition from EDS spectrum

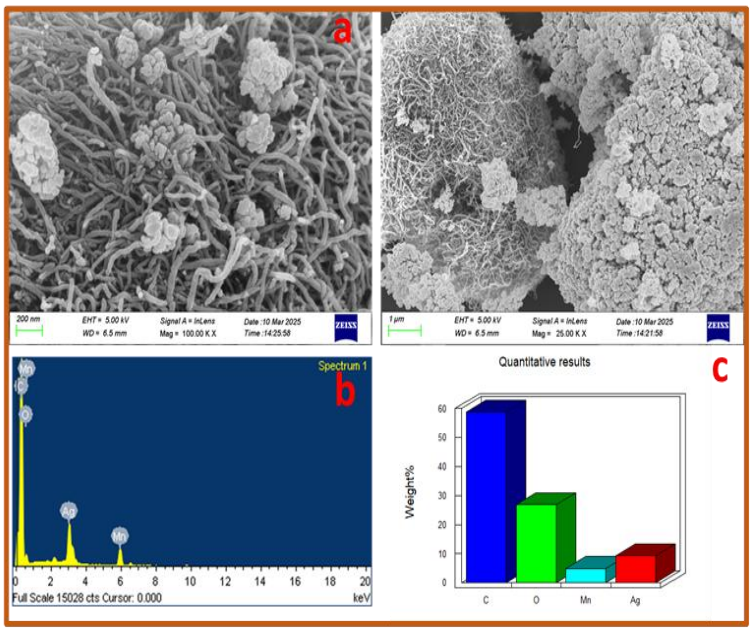

Figure 4. (a) FE-SEM images AMO-MWCNT Nnp, (b) EDS spectrum analysis of AMO-MWCNT Nnp, (c) image corresponding to Graphical representation of Elemental composition from EDS spectrum

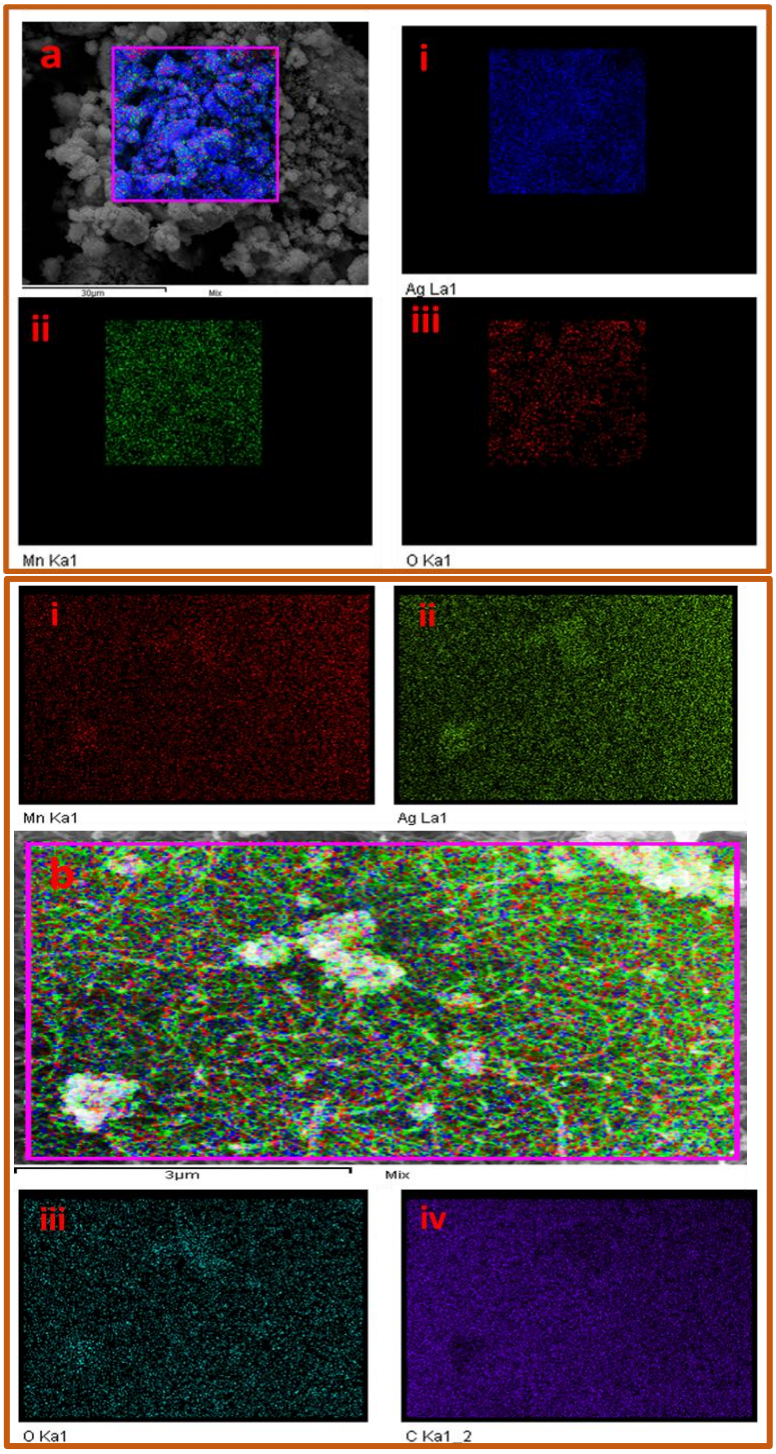

Figure 5. a) Elemental mapping of AMO Nnp i) silver, ii) Manganese, iii) oxygen; b) Elemental mapping of AMO-MWCNT Nnp i) Manganese, ii) silver iii) oxygen, iv) carbon

3.4. Electrochemical studies

3.4.1. Preparation of Modified Glassy Carbon electrodes (GCE)

Before the fabrication process GCE surface was cleaned using alumina particles (0.1M,0.3M,0.05M) then sonicated several times with ethanol and water. A drop of the

prepared AMO Nnp was cast on one electrode surface, AMO-MWCNT Nnp on the other electrode surface. this surface was permitted to air dry at room temperature. After the successful fabrication of both Nnp on GCE was further used to investigate the NEP, UAR, and L-TY sensing performance [35].

3.4.2. Analysis of active surface area of bare GCE, AMO Nnp, and AMO-MWCNT modified GCE

To determine the active surface area of the modified glassy carbon electrode, the electrodes were immersed in a solution containing 10 mM Potassium ferricyanide ($K_3[Fe(CN)_6]$) in 1 M potassium chloride (KCl). As shown in Figure 6, cyclic voltammograms were recorded for bare glassy carbon electrode BGCE (a), AMO Nnp MGCE (b), and AMO-MWCNT (c), respectively. The anodic peak current and redox peak separation are found to be 1.652 µA & 0.320 mV for BGCE, 2.596 µA & 0.279 V for AMO Nnp MGCE, and 3.566 µA & 0.294 mV for AMO-MWCNT Nnp MGCE, respectively. AMO-MWCNT has the highest current response and a large surface area compared to AMO MGCE. When the peak current for the AMO-MWCNT modified electrode increases significantly and the redox peak separation decreases, it suggests an enhanced electron transfer rate and more electroactive sites. The Randles-Sevcik equation (2) is employed to calculate the active surface area of AMO NNp, AMO-MWCNT Nnp MGCE, and BGCE [36].

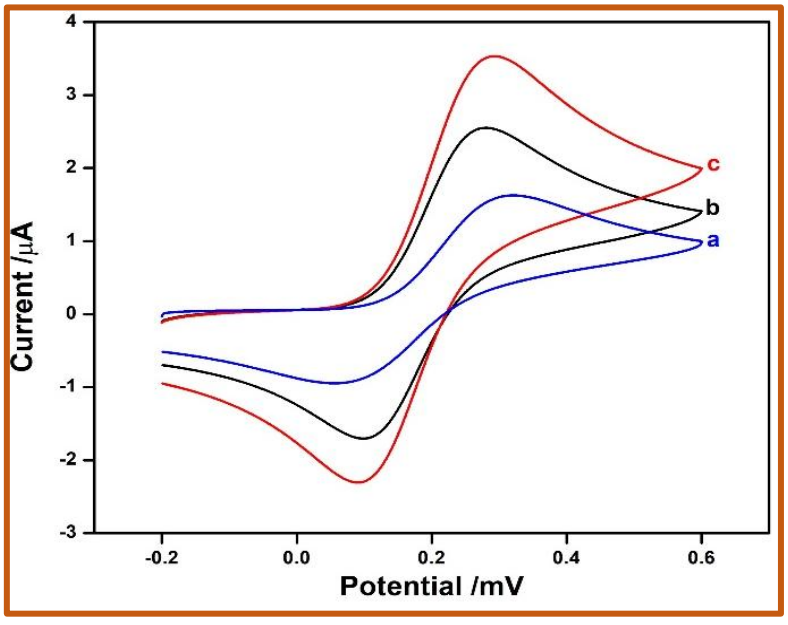

Figure 6. CVs of 10 mM $K_3[Fe(CN)_6]$ in 1 M KCl at AMO-MWCNT Nnp MGCE (a), AMO Nnp MGCE (b), and BGCE (c) with a sweep rate of 50 mV

$$A = I_p / (2.69 \times 10^5)\, n^{3/2}\, D_0^{1/2} C^0 v^{1/2} \quad (2)$$

The active surface area calculations revealed that the BGCE has a surface area of 0.07 cm², whereas the AMO Nnp MGCE 0.12 cm^2 and the AMO-MWCNT Nnp boasts a larger area of 0.22 cm².

3.4.3. Electrochemical behaviour of NEP, UAR and L-TY at BGCE, AMO MGCE, AMO-MWCNT Nnp

By employing the cyclic voltammetry method, the electrochemical properties of the target analytes were detected at both bare and modified electrodes. The cyclic voltammograms (CVs) obtained in the absence of NEP, UAR, and L-TY in 0.2 M phosphate buffer solution (PBS) at pH 7.0 with a scan rate of 50 mV/s at AMO-MWCNT Nnp MGCE are seen in Figure 7 Aa, Ba, Ca. Additionally, in the presence of 25 mM NEP, 25 mM UAR, and 25 mM L-TY at BGCE seen in Figure 7 Ab, Bb, Cb, AMO Nnp MGCE seen in Figure 7 Ac, Bc, Cc, and AMO-MWCNT Nnp seen in Figure 7 Ad, Bd, Cd. Small oxidation peak signals were observed for NEP, UAR, and L-TY at BGCE.

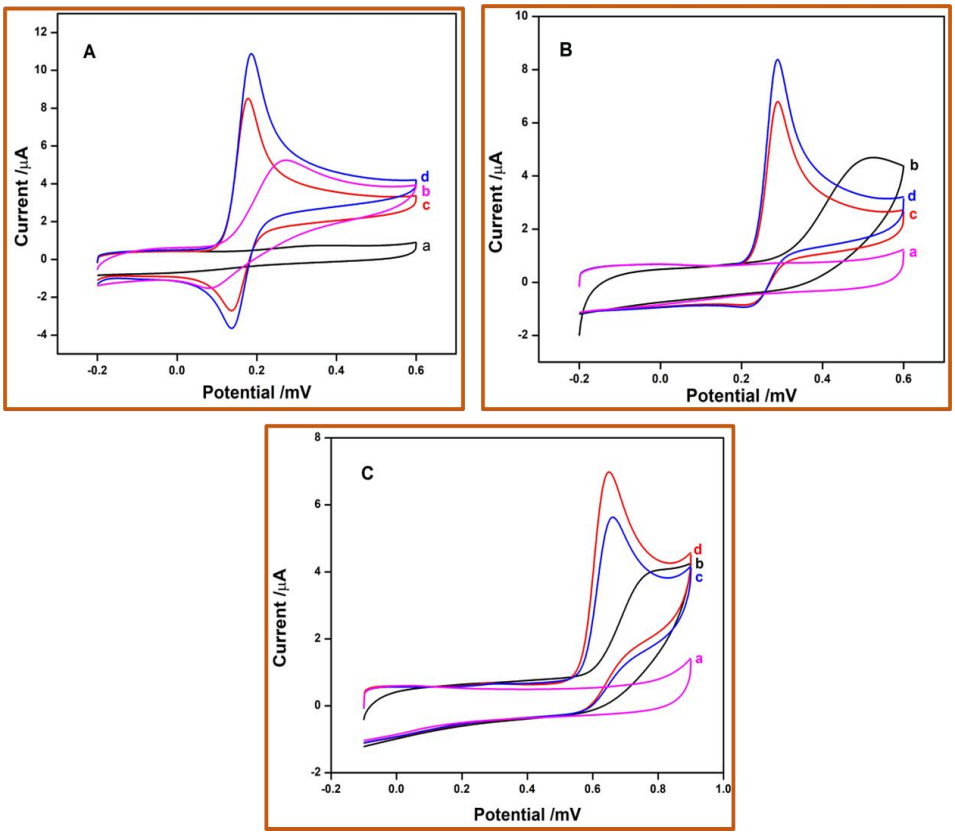

Figure 7. A) CVs in the absence of NEP at AMO-MWCNT Nnp MGCE (a) and BGCE (b), AMO- Nnp MGCE (c), AMO-MWCNT Nnp in presence of NEP; B) CVs in the absence of UAR at AMO-MWCNT Nnp MGCE (a) and BGCE (b), AMO- Nnp MGCE (c), AMO-MWCNT Nnp in presence of UAR; C) CVs in the absence of L-TY at AMO-MWCNT Nnp MGCE (a) and BGCE (b), AMO- Nnp MGCE (c), AMO-MWCNT Nnp in presence of L-TY

Compared to AMO Nnp MGCE, the analytical signals of NEP, UAR, and L-TY are markedly enhanced, and the overpotential is reduced for AMO-MWCNT Nnp modified electrode. The observed increase in peak current can be attributed to the enhanced catalytic efficiency and increased reactive sites of the AMO-MWCNT Nnp MGCE during the electro-oxidation of NEP, UAR, and L-TY compared to AMO Nnp, hence for further parameter AMO-MWCNT Nnp MGCE was used [37].

3.4.4. Effect of pH

The pH of the electrolyte solution significantly impacts electrochemical investigations. The effect of pH on 25 mM NEP, 25 mM UAR, 25 mM L-TY in various pH (4.0, 5.0, 6.0, 7.0, 8.0, 9.0) of 0.2 M PBS at a sweep rate of 50 mV/s was studied using the cyclic voltammetry technique at AMO-MWCNT Nnp MGCE. The cyclic voltammograms NEP exhibit a reversible process, and UAR and L-TY undergo an irreversible process, as shown in Figure 8 (A), (B) and (C). These figures indicate that as pH rises, the peak positions move towards greater negative potentials. At pH 7 both NPE, URA and L- TY show their maximum peak currents. The Figure 8 Ai, Bi, Ci illustrate the linear relationship between potential and pH for NPE, URA, and L- TY respectively. The following are the linear regression equations.
The linear regression equations are as follows:

Ep (NEP)/mV = -0.037 pH + 0.447 (R_2 = 0.934)

Ep (UAR)/mV = -0.024 pH + 0.481 (R_2 = 0.945)

Ep (L-TY)/mV = -0.028 pH+ 0.452 (R_2 = 0.972)

The slopes, measured at -0.037, -0.024, and -0.028 V/pH, respectively, are close to the theoretical value of -0.059 V/pH, indicating that the number of electrons (two) transferred is equal to the number of protons (two H^+ ions) involved in the reaction [38].

3.4.5. Effect of Scan rate

Using the cyclic voltammetry technique, the kinetic properties of the reaction at the AMO-MWCNT Nnp MGCE electrode were analysed, focusing on the effect of scan rate on the voltammetric response for NEP, URA, and L-TY over a potential range of -0.2 to 1.0 V. The peak current increased with the scan rate due to a decrease in the diffusion layer's size. Figure 9 (A), (B), (C) show cyclic voltammograms for 25 mM NEP, 25 mM UAR, 25 mM L-TY in 0.2 M PBS (pH 7.0) at various scan rates from 50 to 500 mV/s, indicating that the oxidation peak current rises with the scan rate.

In Figure 9 Ai, Bi, Ci reveal a relationship between the logarithm of the anodic peak current and the logarithm of the scan rate, with regression equations of:

log (Ip) μA = 0.591 log (ν) mV – 1.032; R^2 = 0.990 for NEP,

log (Ip)μA = 0.313 log (ν) mV + 0.047; R^2 = 0.906 for UAR.

log (Ip)μA = 0.275 log (ν) mV + 0.401; R^2 = 0.947 for L-TY.

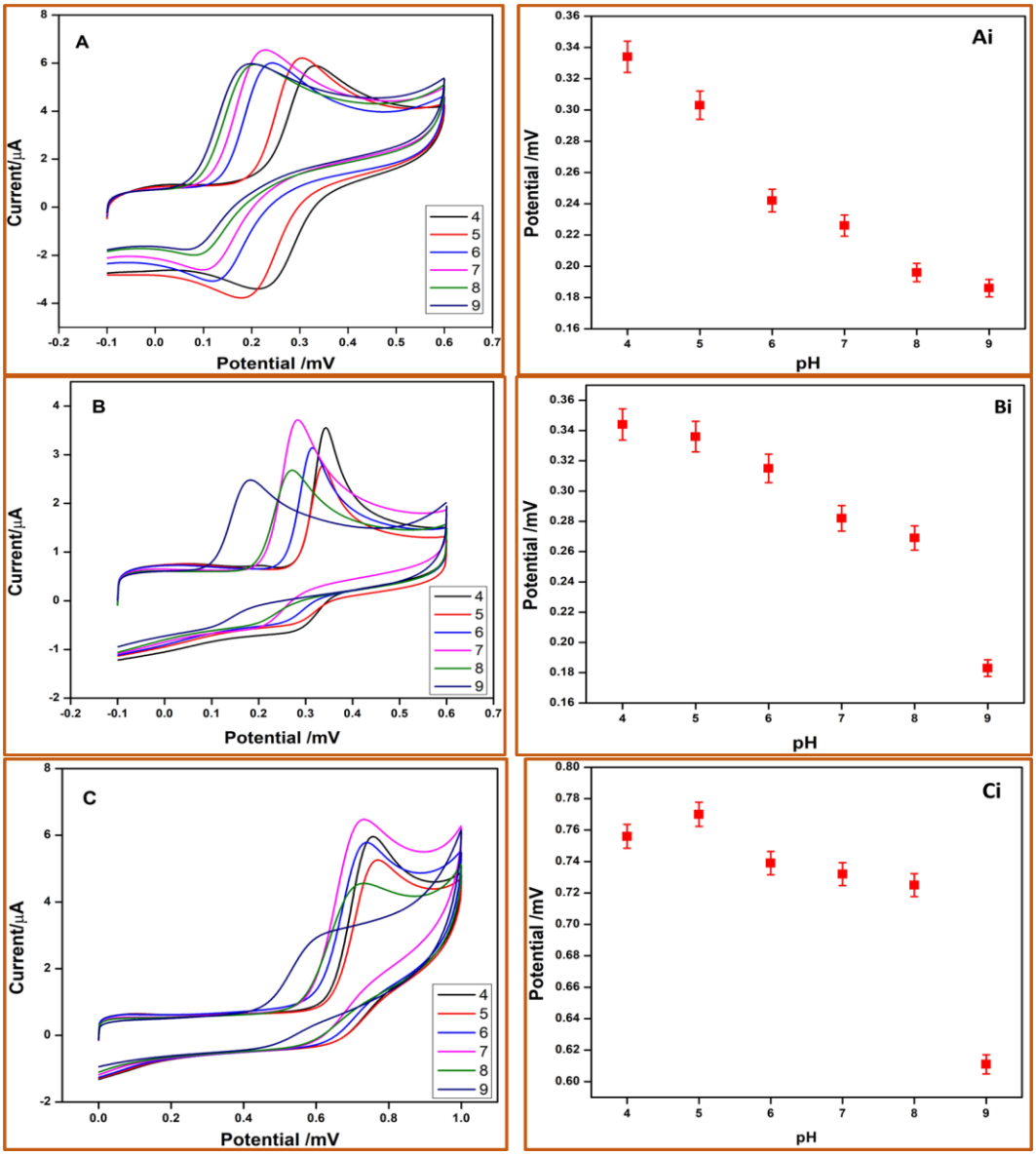

Figure 8. A) CVs of 25 mM NEP recorded at AMO-MWCNT Nnp MGCE in 0.2 M PBS of different buffer pH values (4-9), having a sweep rate of 50 mV. Ai) Calibration plot of pH vs. obtained peak potential of NEP; B) CVs of 25mM URA recorded at AMO-MWCNT Nnp MGCE in 0.2 M PBS of different buffer pH values (4-9), having the sweep rate of 50 mV. Bi) Calibration plot of pH vs obtained peak potential of URA; C) CVs of 25mM L-TY recorded at AMO-MWCNT Nnp MGCE in 0.2 M PBS of different buffer pH values (4-9), having the sweep rate of 50 mV. Ci) Calibration plot of pH vs. the obtained peak potential of NEP

The measured slopes' close proximity to the predicted value of 0.5 for an ideal electrochemical reaction supported by a diffusion-controlled process proves that the electrode behaviour does, in fact, follow a diffusion-controlled sensor process.

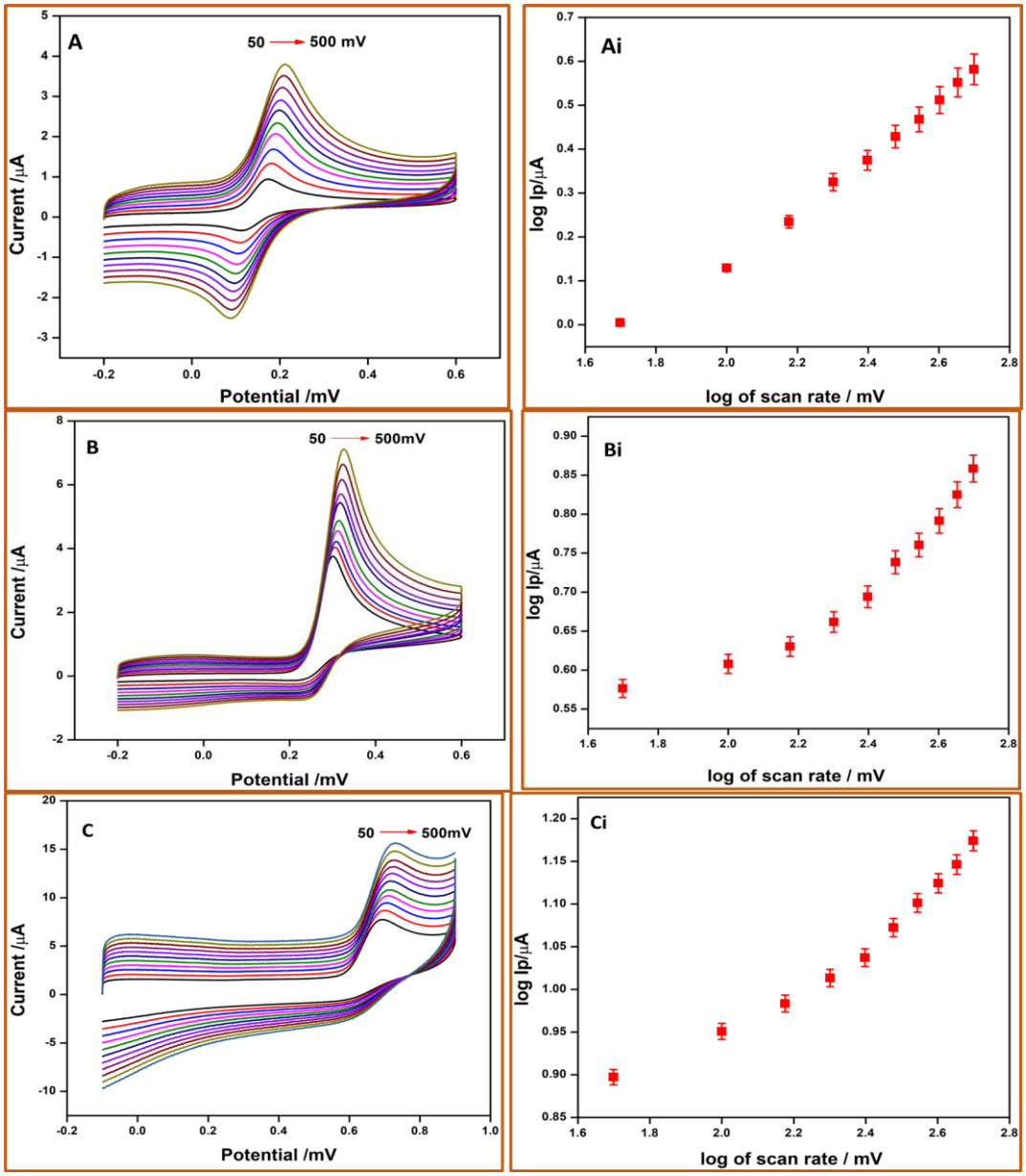

Figure 9. A) CVs of 25 mM NEP in 0.2 M PBS of pH 7.0 with sweep rates (50-500) mV at AMO-MWCNT Nnp MGCE, Ai) Plots of log Ip of v/s log scan rate; B) CVs of 25 mM URA in 0.2 M PBS of pH 7.0 with sweep rates (50-500) mV at AMO-MWCNT Nnp MGCE, Bi) Plots of log Ip of v/s log scan rate; C) CVs of 25 mM L-TY in 0.2 M PBS of pH 7.0 with sweep rates (50-500) mV at AMO-MWCNT Nnp MGCE, **Ci)** Plots of log Ip of v/s log scan rate

3.4.6. Effect of Concentration

DPV demonstrates greater sensitivity compared to CV because it is specifically designed to minimize the background capacitive current generated at the electrode surface as a result of the formation of an electrical double layer in an electrochemical sensor. The quantification of NEP, URA, and L-TY was investigated using differential pulse voltammetry [32].

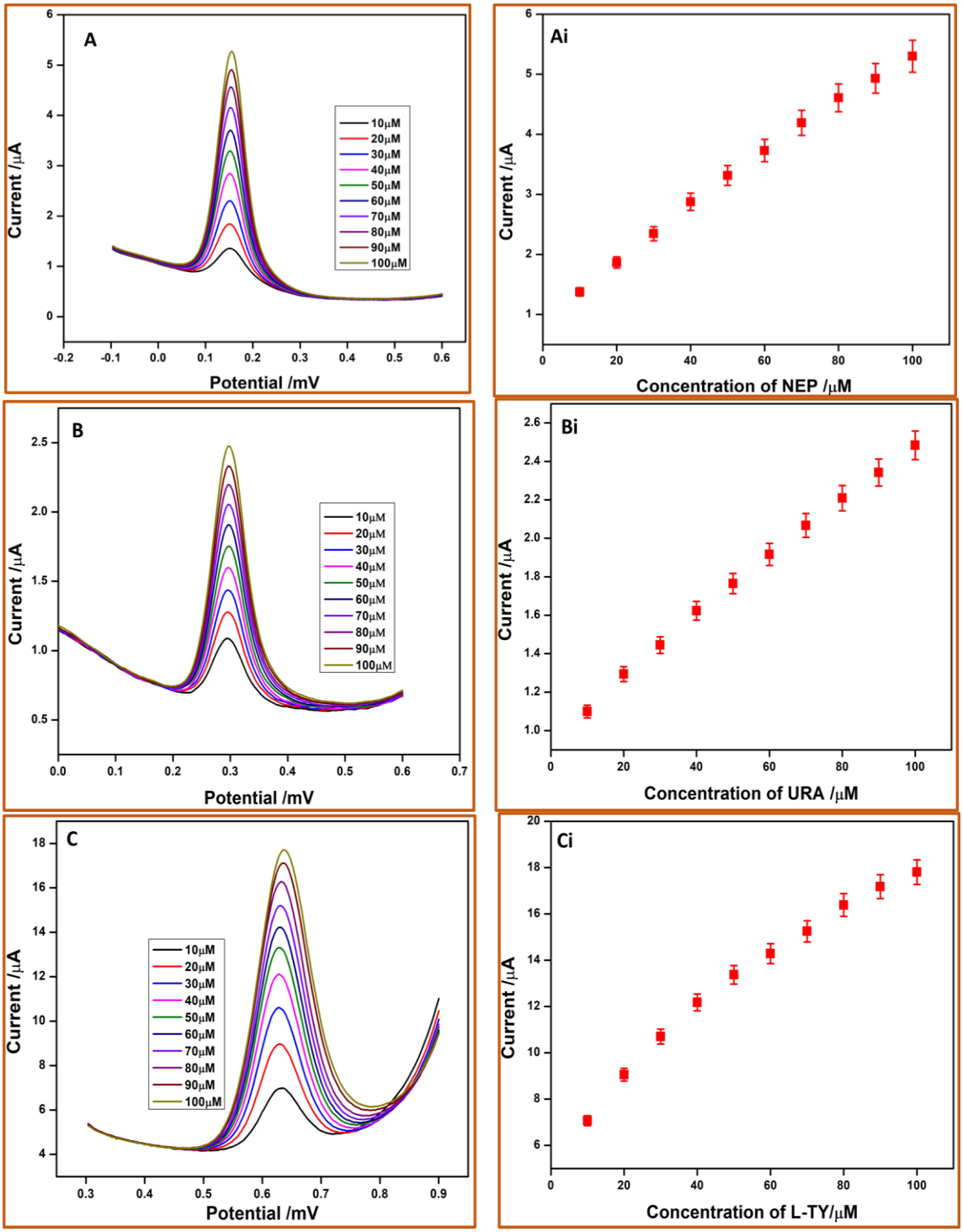

Figure 10. A) DPV curves obtained with different concentrations of NEP on AMO-MWCNT Nnp MGCE in 0.2 M PBS (pH 7.0), Ai) linear plot of current v/s NEP concentration (10 µM-100 µM); B) DPV curves obtained with different concentrations of URA on AMO-MWCNT Nnp MGCE in 0.2 M PBS (pH 7.0), Bi) linear plot of current v/s URA concentration (10 µM-100 µM); C) DPV curves obtained with different concentrations of L-TY on AMO-MWCNT Nnp MGCE in 0.2 M PBS (pH 7.0), Ci) linear plot of current v/s L-TY concentration (10 µM-100 µM)

The voltammetric performance of NEP, URA, and L-TY by varying their concentration was assessed at AMO-MWCNT Nnp MGCE in order to confirm the analytical efficacy. Figure 10 (A, B, C) shows the DPVs for various concentrations from 10 µM to 100 µM NEP, URA, and L-TY, respectively. It was observed that the oxidation peak current increased with an increase in the concentration of NEP, URA, and L-TY. The calibration curve between the Ip vs. C (µM) of NEP, URA, and L-TY was shown to be highly linear in Figure 10 Ai, Bi, Ci, using the linear equations, respectively:

Ip (µA) = 0.043 (µM) + 1.039 (R^2 = 0.995) for NEP

Ip (µA) = 0.015 (µM) + 0.986 (R^2 = 0.997) for URA

Ip (µA) = 0.116 (µM) + 6.923 (R^2 = 0.973) for L-TY.

Table 1. Comparison of AMO/MWCNT Nnp - MGCE with other modified electrodes used to determine

Norepinephrine					
Electrode Material	**Linear range (µM)**	**Method**	**LOD (nM)**	**LOQ (nM)**	**Reference**
MoO_3 NWs /GCE	0.1–2000	DPV	110	330	[39]
$FeMoO_4$ / GCE	0.05–200	DPV	3.7	11.1	[40]
NiO-RGO/ GCE	0.02–14, 14–80	DPV	5	15	[41]
LCys/AuNPs/MWCNTs/ GCE	0.2–100	DPV	30	90	[42]
Fe_3O_4@MCM-48-SO_3H/MWCNTs/GCE	0.4–600	DPV	19	57	[43]
AMO-MWCNT GCE	10-100	DPV	4.4	13.4	Present work
Uric acid					
Electrode Material	**Linear range (µM)**	**Method**	**LOD (nM)**	**LOQ (nM)**	**Reference**
RGO/AuNPs/CSHMs/GCE	1–300	DPV	700	2380	[44]
SnO_2-NP/MWCNTs/CPE	3–200	DPV	100	340	[45]
Mn-SnO_2/GCE	1-860	DPV	36	122.4	[46]
$AgVO_3$ NPs/MGCE	0.1–17	DPV	12.9	43.86	[47]
Fe_xO_y/UNC/GCE	2–200	DPV	290	986	[48]
AMO-MWCNT GCE	10-100	DPV	3.01	10.22	Present work
L-Tyrosine					
Electrode Material	**Linear range (µM)**	**Method**	**LOD (nM)**	**LOQ (nM)**	**Reference**
Zinc oxide/GCE	1.0-800	DPV	500	1670	[49]
MWCNT/GCE	2–500	DPV	400	1336	[49]
Nafion/TiO_2-GR/GCE	10-160	DPV	230	768.2	[50]
Nafion-CeO_2-GCE	2-160	DPV	90	300.6	[51]
MWNTs/4-ABSA modified GCE	0.1-50	DPV	80	267.2	[52]
AMO-MWCNT GCE	10-100	DPV	10.31	34.39	This work

NPs=Nanoparticles, GCE=Glassy carbon electrode, MWCNT=Multiwalled carbon nanotube, RGO=Reduced graphene oxide, DPV=Differential pulse voltammetry

Using Equations (3) and (4), the limit of detection and quantification limits were suggested. The LOD and LOQ for NEP were 4.04 nM and 13.40 nM, for URA 3.01 nM and 10.22 nM, and for L-TY 10.31 nM and 34.39 nM, respectively.

$$LOD = 3\ S/M \quad (3)$$

$$LOQ = 10\ S/M \quad (4)$$

The enhanced sensitivity of the electrode and its decreased detection limit indicated a notable improvement in the AMO MWCNT Nnp surface's electroactivity towards NEP, URA, and L-TY. This progression can be attributed to the material's superior conductivity and electrocatalytic properties, which facilitated achieving a lower detection limit.

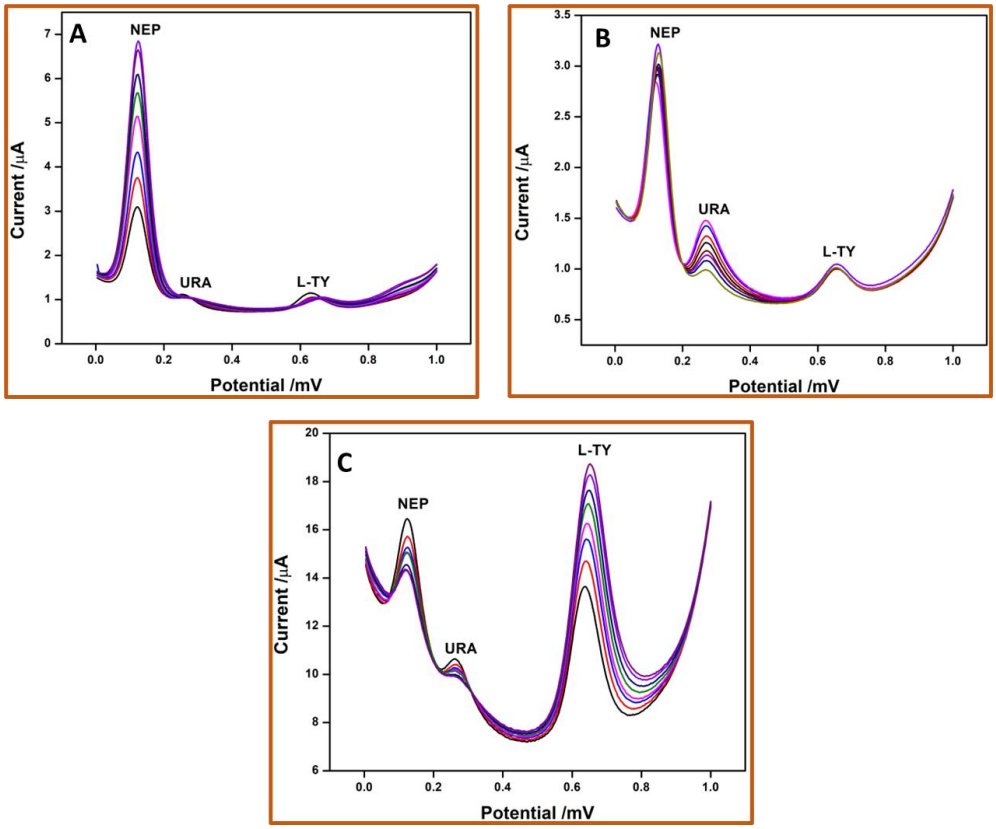

Figure 11. A) DPVs of NEP (10 to 80 µM) in 0.2 M PBS of pH 7 with 10 µM URA and 10 µM L-TY with a Scan rate of 50 mV at AMO-MWCNT Nnp MGCE; B) DPVs of UAR (10 to 80 µM) in 0.2 M PBS of pH 7 with 10 µM NEP and 10 µM L-TY with a Scan rate of 50 mV at AMO-MWCNT Nnp MGCE; C) DPVs of L-TY (10 to 80 µM) in 0.2 M PBS of pH 7 with 10 µM NEP and 10 µM UAR with a Scan rate of 50 mV at AMO-MWCNT Nnp MGCE

3.4.7. Simultaneous detection of NEP, URA and L-TY

The DPV technique was used to accomplish the simultaneous analysis in the mixture of NEP, URA, and L-TY samples at the AMO MWCNT Nnp MGCE by maintaining one of the

mixture's constituents at a fixed concentration and altering another. Various NEP concentrations (10–80 µM) at AMO-MWCNT Nnp MGCE with a sweep rate of 50 mV/s while maintaining a constant URA and L-TY concentration in the presence of 0.2 M PBS at pH 7.0, are shown in Figure 11A. Furthermore, whereas NEP and L-TY concentrations remain constant and the URA concentration varies between 10 and 80 µM in Figure 11B, after that, the concentration of L-TY is varied between 10 and 80 µM while maintaining a constant concentration of NEP and URA the corresponding peak is displayed in Figure 11C.

3.4.8. Real sample analysis

To evaluate the practical applicability of the electrode, the AMO-MWCNT MCPE was utilized to analyse a commercially available Norepinephrine Bitartrate injection, containing NEP at a concentration of 1 mg/mL. The injection samples were appropriately diluted in 0.2 M phosphate buffer solution (PBS, pH 7.0) to achieve a final concentration of 2.5 mM. The standard addition method was employed to quantify NEP in pharmaceutical formulations. Sample analysis was conducted using repeated cyclic voltammetry measurements (n = 3) on diluted preparations spiked with known concentrations of NEP. The results, summarized in Table 2 indicate recoveries ranging from 98.9% to 101.7%. These findings highlight the remarkable sensitivity of the AMO-MWCNT MGCE in detecting NEP within pharmaceutical samples.

Table 2. Detection of NEP in injection sample(n=3)

Sample	**Added (µM)**	**Found (µM)**	**Recovery %**
NEP Injection	1	0.989	98.9%
	2	1.991	99.5%
	3	3.051	101.7%

4. CONCLUSION

Silver manganese oxide (AMO) nanoparticles were synthesized via the coprecipitation method. XRD analysis confirmed their crystallinity, revealing average particle sizes of 32 nm for pure AMO Nnp and 27 nm when combined with MWCNTs. The resulting AMO-MWCNT Nnp composite was used to fabricate a highly stable, sensitive, and selective modified glassy carbon electrode for the electrochemical detection of NEP, URA, and L-TY. Cyclic voltammetry was employed to study the electrochemical behaviour of the AMO-MWCNT Nnp modified glassy carbon electrode for simultaneous detection of these analytes. The composite exhibited a large surface area, excellent conductivity, and high peak currents, indicating strong catalytic activity toward analyte oxidation. The sensor demonstrated a broad linear response range, along with high stability and sensitivity. Under optimal conditions, it achieved

remarkably low limits of detection and quantification for NEP, URA, and L-TY. Additionally, the AMO-MWCNT Nnp sensor was successfully applied to detect NEP in a pharmaceutical sample, yielding accurate and reliable results.

Declarations of interest

The authors declare no conflict of interest in this reported work.

REFERENCES

[1] S. Renjini, P. Abraham, V.A. Kumary, P.G. Chithra, and K. Sreevalsan, Journal of The Electrochemical Society 169 (2022) 046519.

[2] M. Su, X. Cao, H. Gao, C. Zhu, W. Peng, Q. Jiang, and C. Yu, Analytica Chimica Acta 1262 (2023) 341247.

[3] J. Chen, H. Huang, Y. Zeng, H. Tang, and L. Li. Biosensors and Bioelectronics 65 (2015) 366.

[4] F. Fallah, M.R. Shishehbore, and A. Sheibani. Talanta 252 (2023) 123776.

[5] M. Cui, Y. Feng, D.J McAdoo, and W.D. Willis. The Journal of pharmacology and experimental therapeutics 289 (1999) 868.

[6] S.W. Cole, Y.D. Korin, J.L. Fahey, and J.A Zack, The Journal of Immunology 161 (1998) 610.

[7] D. Voet, and J.G. Voet, Nucleotide metabolism. New York: John Wiley & Sons (1995). 795.

[8] S.Y. Ly, Y.H. Kim, I.K. Han, I.G. Moon, W.W. Jung, S.Y. Jung, H.J. Sin, T.K. Hong, and M.H. Kim, Microchemical Journal 82 (2006) 113.

[9] B.R. Putra, U. Nisa, R. Heryanto, E. Rohaeti, M. Khalil, A. Izzataddini, and W.T. Wahyuni, Analytical Sciences 38 (2022)157.

[10] J. Maiuolo, F. Oppedisano, S.Gratteri, C. Muscoli, and V. Mollace, International Journal of Cardiology 213 (2016) 8.

[11] M.M. Rahman, N.S. Lopa, K. Kim, and J.J. Lee, Journal of Electroanalytical Chemistry, 754 (2015) 87.

[12] M. Pari, and K.R.V. Reddy, Anal. Bioanal. Electrochem. 11 (2019) 1383.

[13] W. Hu, D. Sun, and W. Ma, Electroanalysis 22 (2010) 584.

[14] Y. Liu, X. Sun, D. Di, J. Quan, J. Zhang, and X. Yang, Clinica Chimica Acta 412 (2011) 2132.

[15] M. Mamiński, M. Olejniczak, M.Chudy, A. Dybko, and Z. Brzózka, Analytica Chimica Acta 540 (2005) 153.

[16] A. Makrlíková, F. Opekar, and P. Tůma, Electrophoresis 36 (2015) 962.

[17] J.C. Fanguy, and C.S. Henry, Electrophoresis 23 (2002) 767.

[18] X. Fang, H. Ren, H. Zhao, and Z. Li, Microchimica Acta 184 (2017) 415.

[19] D.E. Matthews, The Journal of Nutrition 137 (2007) 1549S.
[20] K.J. Huang, D.F. Luo, W.Z. Xie, and Y.S. Yu, Colloids and Surfaces B: Biointerfaces 61 (2008) 176.
[21] S.M. Ghoreishi, M. Behpour, N. Jafari, and M. Golestaneh, Journal of the Chinese Chemical Society 59 (2012) 1015.
[22] G.P. Jin and X.Q. Lin, Electrochemistry Communications 6 (2004) 454.
[23] A. Carlsson, and M. Lindqvist, Naunyn-Schmiedeberg's Archives of Pharmacology 303 (1978) 157.
[24] N. Hareesha, J.G.G. Manjunatha, C. Raril, and G. Tigari, Advanced Pharmaceutical Bulletin 9 (2019) 132.
[25] S.Y. Ly, Y.H. Kim, I.K. Han, I.G. Moon, W.W. Jung, S.Y. Jung, H.J. Sin, T.K. Hong and M.H. Kim, Microchemical Journal 82 (2006) 113.
[26] J. Li, D. Kuang, Y. Feng, F. Zhang, and M. Liu, Microchimica Acta 176 (2012) 73.
[27] G. Tigari, Z. Yhobu, S. Budagumpi, and R.S. Keri, Inorganic Chemistry Communications 158 (2023) 111593.
[28] B. Habibi, H. Pezhhan, and M.H. Pournaghi-Azar, Microchimica Acta 169 (2010) 313.
[29] J. Li, D. Kuang, Y. Feng, F. Zhang, and M. Liu, Microchimica Acta 172 (2011) 379.
[30] J.M. George, A. Antony, and B. Mathew, Microchimica Acta 185 (2018) 1.
[31] N. Koriche, R. Brahimi, B. Bellal, and M. Trari, Russian Journal of Electrochemistry 58 (2022) 634.
[32] T. Liu, Z. Lai, J. Liu, Q. Yu, X. Liu, Y. Zheng, and X. Li, Journal of Alloys and Compounds 911 (2022) 164.
[33] R. Rathnasamy, and V. Alagan, Physica E: Low-dimensional Systems and Nanostructures 102 (2018) 146.
[34] R.B. Anagawadi, and K.R. Mahanthesha, Results in Chemistry 7 (2024) 101479.
[35] N.S. Devi, P. Rekha, C.P. Lorena, V.S. Patricia, A.H. María, R.R. Devi, and S. Thanikaikarasan, Journal of Food Measurement and Characterization 18 (2024) 1238.
[36] G. Tigari, J. G. Manjunatha, J. G. Nagarajappa, A. M. Tighezza, M. D. Albaqami, and M. Sillanpaa, Journal of Food Measurement and Characterization 18 (2024) 1238.
[37] L.A. Adnan, N.F. Alheety, A.H. Majeed, M.A. Alheety, and H. Akbaş, Materials Today: Proceedings 42 (2021) 2700.
[38] K.M. Pallavi, G.P. Mamatha, G. Nagaraju, and T.L. Soundarya, Inorganic Chemistry Communications 158 (2023) 111427.
[39] K. J. Samdani, D. W. Joh, M. K. Rath, and K. T. Lee, Electrochimica Acta 252 (2017) 268.
[40] K. J. Samdani, J. S. Samdani, N. H. Kim, and J. H. Lee, Biosensors and Bioelectronics 81 (2016) 445.

[41] M. Su, X. Cao, H. Gao, C. Zhu, W. Peng, Q. Jiang, and C. Yu, Analytica Chimica Acta 1262 (2023) 341247.
[42] S. Mukdasai, V. Langsi, M. Pravda, S. Srijaranai, and J. D. Glennon, Sensors and Actuators B 236 (2016) 126.
[43] A. Yousefi, and A. Babaei, Ionics 25 (2019) 2845.
[44] X. Liu, L. Pan, T. Lv, Z. Sun, and C. Q. Sun, Journal of Colloid and Interface Science 408 (2013) 145.
[45] Sun, Daming, Qian Zhao, Feng Tan, Xiaochun Wang, and Jinsuo Gao, Analytical Methods 10 (2012) 3283.
[46] N. Lavanya, N. Fazio, E. F. Neri, A. Bonavita, S. G. Leonardi, G. Neri, and C. Sekar, Journal of Electroanalytical Chemistry 770 (2016) 2332.
[47] K. M. Pallavi, G. P. Mamatha, G. Nagaraju, and C. Mallikarjunaswamy, Russian Journal of General Chemistry 94 (2024) 406.
[48] A. A. Hathoot, K. M. Hassan, W. A. Essa, and M. Abdel-Azzem, Journal of the Iranian Chemical Society 14 (2017) 1789.
[49] P. Norouzi, H. Salimi, S. Tajik, H. Beitollahi, M. Rezapour, and B. Larijani, International Journal of Electrochemical Science 12 (2017) 5254.
[50] Y. Fan, J. H Liu, H. T.Lu, and Q. Zhang, Microchimica Acta 173 (2011) 241.
[51] A. S. Razavian, S. M. Ghoreishi, A. S.Esmaeily, M. Behpour, L. M.Monzon, and J. M. D. Coey, Microchimica Acta 181 (2014) 1947.
[52] K. J. Huang, D. F. Luo, W. Z. Xie, and Y. S. Yu, Colloids and Surfaces B: Biointerfaces, 6 (2008) 176.